A Highly Compact 530-610 GHz Bandpass Filter Using Patch Resonators to Develop SSB Spectrometer

Berhanu T Bulcha[1], Diego Tononi[2], Thomas Stevenson[1], Edward J. Wollack[1]
NASA Goddard Space Flight Center, Greenbelt MD, 20721, USA
Blue Origin, Highlands Ranch, CO, 80129, USA

***Abstract* — In double sideband (DSB) receiver systems, both the desired signals and unwanted image frequencies are downconverted, necessitating effective filtering to enhance system selectivity and sensitivity. This manuscript presents a novel submillimeter-wave bandpass filter optimized for the spectral detection of key atmospheric constituents, including water vapor ($H_2{}^{16}O$ – 559.9 GHz), deuterium oxide (HDO – 539.0 GHz), and oxygen (O_3 – 570.1 GHz) within the 530-610 GHz spectral range. This design employs compact triangular microstrip patch resonators that achieve sharp roll-off characteristics and wide stopband performance, making it ideal for image rejection applications across submillimeter-wave and THz bands. The filter is fabricated on a 15 µm quartz substrate with 0.5 µm gold metallization, providing a 3 dB bandwidth of approximately 80 GHz with well-defined rejection bands below 530 GHz and above 610 GHz. Signal coupling is accomplished through microstrip waveguide feed probes for input and output. The design methodology offers significant flexibility, allowing straightforward scaling and adjustment of center frequency and bandwidth for implementations ranging from 1 GHz to 2 THz. The versatility of the filter architecture presented has utility in radio astronomy, defense systems, and high-frequency communication network applications.**

***Index Terms*— Submillimeter-wave Component, Terahertz, Bandpass Filter, Patch Resonator**

I. Introduction

Spectrocopy enables the characterization of the interactions between matter and light and enables *in situ* identification of elemental and molecular specices from their spectral signatures.

Manuscript received xxx 2025; revised xx; accepted xx. Date of publication xxx; date of current version xxx. This article was recommended by xxx.
(Corresponding author: Berhanu Bulcha, berhanu.t.bulcha@nasa.gov)
Berhanu Bulcha, Thomas Stevensonand Edward J. Wollack are with the NASA Goddard Space Flight Center, Greenbelt, MD 20771, USA.
Diego Tononi is Blue Origin, Highlands Ranch, CO, 80129, USA
Color versions of one or more figures in this article are available at xxx.
Digital Object Identifier xxxxx

In the submillimeter, spectrometers have demonstrated their effectiveness as remote sensing tools for the investigation of volatile compounds, particularly water, and its isotopologues, as well as ices and condensates within various environments throughout the solar system and beyond. The forthcoming generation of spectrometers is anticipated to provide detailed analysis of the atmospheres of gas giants, terrestrial planets, comets, satellite plumes, and asteroid exospheres, thereby contributing essential data regarding their composition and dynamics. As part of the technology maturation process, reduction to the size, weight, and power (SWAP) characteristics of submillimeter-wave spectrometers through simplified design approaches will render them more suitable for future space missions. Spectrometers designed with front-end electronics that implement a single-sideband (SSB) receiver architecture—using filters instead of hybrid couplers and image rejecting mixers (e.g., see discussion in [18]) —bring numerous advantages. These include a) image rejection capabilities that effectively eliminate or attenuate unwanted signal interference and noise, b) improved selectivity of a frequency band by limiting bandwidth, allowing for more targeted measurements, c) enhanced sensitivity resulting in superior quality spectroscopic data, and d) a more compact and integrated system architecture.

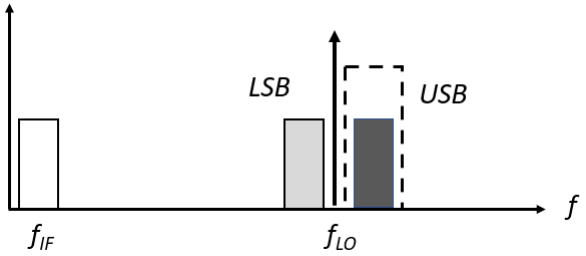

Figure 1: Receiver frequency down-conversion of USB and LSB for single-side and double-side scenarios.

Figure 1 illustrates the Local Oscillator (ω_{LO}) alongside the radio frequency bands depicted as Upper Sideband (USB) and Lower Sideband (LSB) regions. The architecture of the DSB receiver facilitates the down-conversion of both the USB (ω_{RF}) and LSB (ω_{Image}) to a similar Intermediate Frequency (ω_{IF}) that operates at a significantly reduced frequency for spectroscopy data processing, (refer to Eqn. 1 and Eqn. 2).

Consequently, the combination of these two down-converted products results in a doubling of the IF noise, adversely impacting the sensitivity of the instrument.

$$\omega_{IF} = Acos(\omega_{RF} - \omega_{LO}) \quad \text{Eqn. (1)}$$

$$\omega_{Image} = Acos(\omega_{RF} - 2\omega_{IF}) \quad \text{Eqn. (2)}$$

A bandpass filter can be employed to removed the image frequency band and reject spurious signals, improving receiver selectivity and sensitivity. See Figure 1. The dotted line around the USB represents the bandpass filtering that only allows the USB signal and rejects the LSB. Thus, the down-converted IF signal will only be associated with the USB.

Waveguide filters with periodic irises, cavities, or E-plane stubs, which form resonance elements, are readily available for frequencies below 200 GHz and are mainly manufactured using a Computer Numerical Control (CNC) tooling [7]. However, this technique faces numerous challenges as the demand for high-frequency (shorter-wavelength) components has increased above 300 GHz for various applications, including astronomy, communications and military. For many submillimeter-wave components, such as periodic cavity or irises filters, critical features require < 2% errors to realize the desired filter response. Generally, the CNC technique provides a +/- 10 µm precision, which leads to approximately 3-7% machining error at 500 GHz and more than 10% error for frequencies above 1 THz (Figure 2). One of the primary challenges in this spepctral regima is achieving the desired waveguide dimensional precision of +/-2 µm and approapriate surface finish at a reasonable cost.

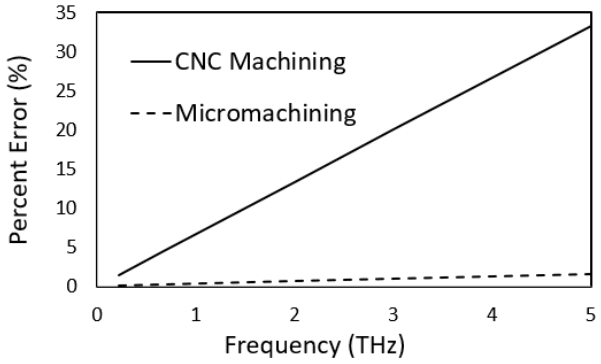

Figure 2: Estimated percent of error for CNC and micromachining techniques in the submillimeter and THz range.

Previous technologies have successfully demonstrated the application of micromachined filters for frequencies above 400 GHz on degenerately doped silicon to define critical structures precisely [8]. The waveguide resonant cavity structures are fabricated within the Silicon-on-Insulator (SOI) device layer by utilizing a photo-sensitive polymer to create a specific pattern. Subsequently, the SOI device layer undergoes etching through a deep reactive ion etch (DRIE) process, which halts at the internal silicon dioxide layer. The micromachining technique enabled the precise definition of the filter channel depth at sub-micrometer scales by carefully controlling the thickness of the SOI device layer, resulting in an error margin of less than 1%. Nevertheless, this approach encounters challenges in maintaining vertical sidewalls for deep-trenched structures, which may hinder the attainment of the desired filter performance [9 - 12].

There is a lack of filters above 300 GHz with a simpler fabrication approach that provides sharp roll-off to suppress the image signal from receivers. Most SSB receivers are implemented using a complex receiver architecture, such as Band Separation (BS) or Image Rejection (IR) techniques. These approaches incorporate multiple 90-degree Hybrid Couplers and mixers to eliminate the unwanted frequency bands relying on phase cancellation. In addition to the complexity of this technique, it increases the size and cost, which is undesirable for space applications, further discussions could be found in [18] and [19].

To address this challenge, a novel submillimeter-wave compact filter utilizing triangular patch resonators is designed, fabricated, and tested to develop SSB receiver systems. The filter passband is 530-610 GHz, allowing only the USB and rejecting the LSB of the receiver. The presented filter design can be utilized to meet the demands of the newer-generation communication industry, which requires improvements in selectivity and the proper utilization of the communication spectrum while enforcing a compact, low-cost design with low insertion loss.

II. Filter Design

The developed filter employs isosceles triangle-patterned elements, each featuring two equal-length sides [4].

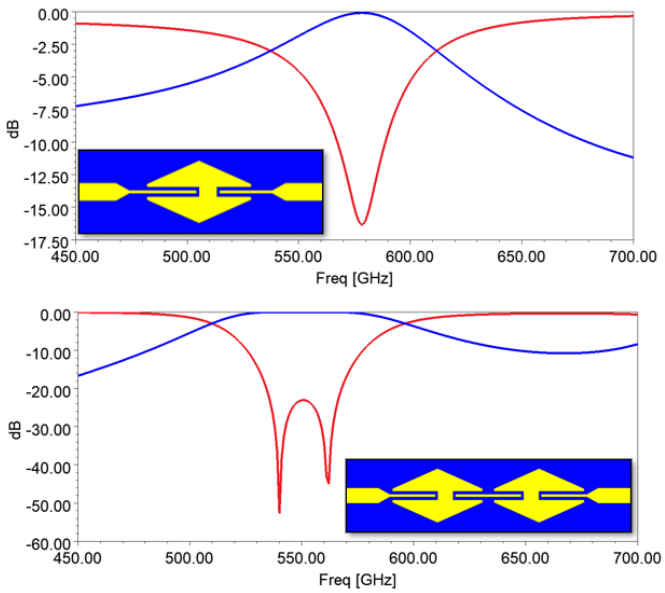

Figure 3: A single and double pi-networks patch filter designs and their corresponding parameter responses.

Each triangle patch features a half-wave resonator, contributing to a multipole resonating filter design. A 0.5 µm thick gold was deposited as a conductive layer on a thin quartz substrate to realize these patches. The relatative permittivity of the quartz dielectric substrate, approximately $\varepsilon_r \sim 4$ [19], facilitates a reduction in the effective length of the resonator. The initial phase of our design involved creating a lower-order, a single pi-network filter composed of two symmetrically positioned triangular patches coupled to an inductive probe. The resulting design (refer to Figure 3, top) exhibited a bandpass filter characteristic with a center frequency of approximately 575 GHz.

This lower-order filter displayed a roll-off rate of 15 dB/Octave and demonstrated limited rejection outside the specified band. We increased the filer order to enhance outside band rejection performance; thus, the number of pi-networks with triangular patches that are coupled capacitively with an inductive line is doubled. The resultant S-parameter response (Figure 3, bottom) illustrates a well-defined bandpass. The center frequency has shifted by 25 GHz from the lower order filter to 550 GHz due to incorporating additional inductive structures between the two pi-networks. This increase in the filter's order and resulted in an improved roll-off rate of 45 dB/Octave. We further extended the design to include six triangular patches by adding a parallel half-wave resonator to refine the filter's roll-off characteristics for the intended application (see Figure 4 (bottom). Each resonator comprises nearly equal-sized triangular structures, with the optimization process yielding a size difference between W_1 and W_2 of less than 1 µm. An inductive finger capacitively couples the electric field from the probe to the triangular structures, while the capacitive coupling among them establishes a high-pole resonance filter. As a result, the design achieves an ultrawide transmission zero, with a sharp roll-off response exceeding 60 dB/Octave.

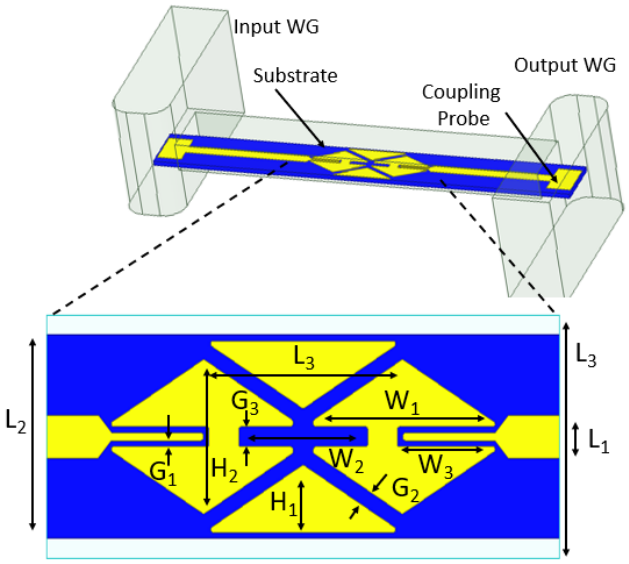

Figure 4: (Top) HFSS model of a six triangular patch filter including the coupling probes embedded in a waveguide structure, (Bottom) filter's design and dimensions optimized for a center frequency of 570 GHz with 80 GHz, 3 dB bandwidth.

To couple a high-frequency electromagnetic wave to the filter microstrip structure, a WM-380 standard metallic waveguide for the 500-750 GHz operation with dimensions of a = 380 µm and b = 190 µm is implemented. A waveguide probe is incorporated into the filter design, creating an impedance-matching transition between the E-plane waveguide split-block and the microstrip mode. The filter's critical parameters and optimized values are shown in Table 1.

Figure 4 shows the complete circuit design integrated with an input and output coupling probe with dimensions of 80 x 110 µm. The probe is recessed by 5 µm and 23.5 µm from the front and to the side, respectively, onto the substrate. The circuit, including the input/output probes, has a total length of 1.4 mm and features a 90 µm air suspension on both sides of the probe adjacent to the waveguide.

Table 1: Critical design parameters and dimensions of a six triangular patch, higher order bandpass filter.

Parameter	Dimensions (µm)	Parameter	Dimensions (µm)
W_1	200	G_1	6
W_2	201	G_2	15
W_3	140	G_3	16.5
W_4	101	L_1	30
H_1	100	L_2	143
H_2	107	L_3	201

The input and output circuit channels and substrate dimensions have been meticulously optimized to achieve single-mode excitation within the designated frequency band. This optimization is crucial in order to mitigate the excitation of multiple waveguide modes within the filter structure, which can disrupt the performance of the patch resonators and adversely affect the filter response. Figure 5 illustrates a simulation using the High-Frequency Structure Simulator (HFSS), demonstrating the attenuation (α) of the first five waveguide modes.

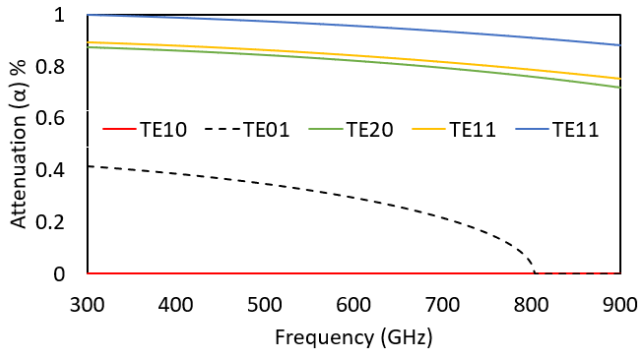

Figure 5: A simulated attenuation versus frequency for waveguide mode within the designed circuit channel.

The primary waveguide mode, TE10, propagates without experiencing any attenuation. Conversely, the remaining modes

exhibit attenuation, with the second mode becoming active at approximately 820 GHz, which lies outside the intended frequency of 750 GHz. The optimization process led to the adoption of an enclosure with deminsions of 183.5 × 91.5 × 91.5 µm for the filter circuit on a quartz substrate having a width of 143 µm and thickness of 15 µm.

Figure 6 illustrates the surface current distribution (*J*) of the six-pole filter design for in-band operation at 570 GHz and out-of-band operation at 500 GHz. The surface current shows resonance created within each isosceles triangle and their coupling. At 570 GHz, at the center of the passband, the surface current contour is well distributed as the wave travels from input to output ports, showing a transmission property. However, the surface current is disrupted outside the frequency band, near 500 GHz, and energy is reflected.

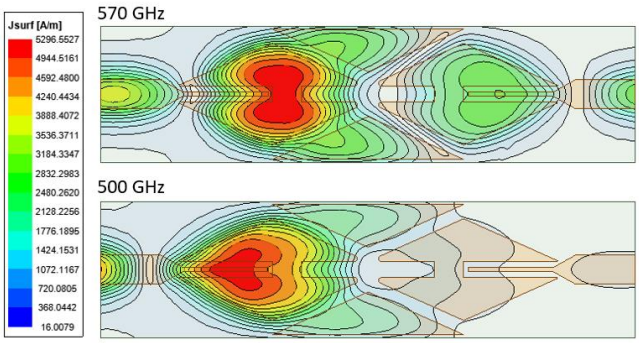

Figure 6: Surface current (***J***) distribution simulated at 500 GHz and 570 GHz.

Figure 7 illustrates a simulated performance of a six triangular patch filter design arranged in a pi-networks. The filter exhibits a sharp roll-off and low loss in the transmission band, offers transmission zeros on either side of the passband, and provides excellent rejection of outside-band spurious signals.

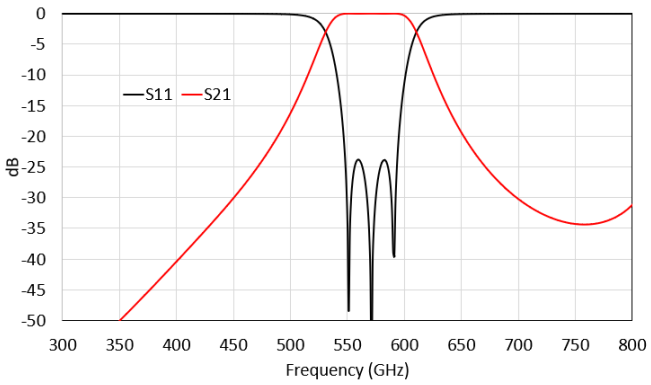

Figure 7: HFSS simulated filter performance, all parameters are optimized, less dielectric losses and perfect-E metallization.

Changing the critical parameters makes the design agile for scalability and tunability for other frequencies in the 1 GHz to 2 THz range. For a small bandwidth tunability (10 % or less) and shifting center frequency, parameters such as G_1 and the distance between any two triangles (G_2) will change the bandwidth while moving the center frequency. Changing the isosceles triangle dimensions, H_1 and W_1, while optimizing the spacing, G1 and substrate height will drastically shift the center frequency. To change the filter design with different substrate materials such as Roger 3003 ($\varepsilon_r = 3$), Alumina ($\varepsilon_r = 9.4$), GaAs ($\varepsilon_r = 11.9$) for lower frequency applications, the substrate height (h), width (w) and the dielectric constant (ε) need to be factored into Equation 3, Hammerstad and Jensen microstrip model [5, 6], while maintaining a 50-ohm impedance at the input and output of the microstrip lines, L_1.

$$Z_0 = \frac{120\pi}{\sqrt{\varepsilon_{eff}\left({}^{w}/_{h}+1.393+0.667\ln\left({}^{w}/_{h}+1.444\right)\right)}}\ (\Omega) \quad \text{Eqn. (3)}$$

Figure 8 shows an equivalent lumped element circuit for the final design that provides further insight into the functional elements of the transmission line structure and its response. The two pi-networks consisting of inductor L_3 flanked by two capacitors of value C_3 represent the left- or right-hand pairs of triangular patches, each acting as a half-waver resonator. A third half-wave resonator is the parallel combination of the middle two triangular patches, represented by the pi-network with L_4 and C_4. The ladder networks involving L_1, C_0, and C_1 serve as transformers, which transform the 50 Ω port impedance up to a level (≈ 375 Ω) that gives the following half-wave resonator the appropriate quality factor for the desired filter bandwidth. The two capacitors C_2 joining the three resonators provide sufficient coupling to make the three resonances merge, while slightly adjusting the resonance frequency of the middle resonator allows passband ripple to be minimized. The circuit values (L_1 = 31.0, L_3 = 27.6, L_4 = 29.1 pH, and C_0 = 2.20, C_1 = 2.30, C_2 = 0.97, C_3 = 4.95, C_4 = 4.56 fF) are close to simple estimates based on the length, area, and general taper of the geometric elements represented.

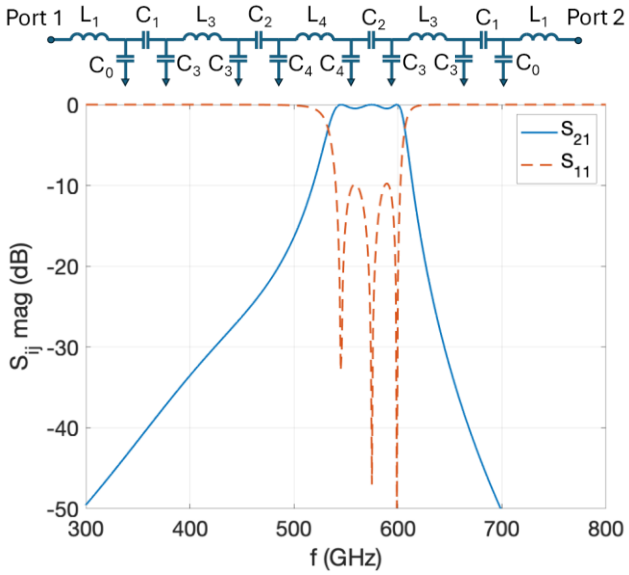

Figure 8: An equivalent lumped element circuit representing the filter shows similar band pass performance in its S-parameters. The circuit consists of input and output impedance transformers and a chain of three resonant pi-networks joined by series coupling capacitors.

The lumped element circuit reproduces the center frequency, bandwidth, and roll-off on the low frequency side seen in the 2D simulation. The lumped element circuit does not include the second harmonics of the patch resonators, which softens the high-frequency roll-off.

III. Filter Fabrication and Assembly

A photomask was created with the filter design, followed a standard planar circuit fabrication approach, and was fabricated to deposit a thin gold, 0.5 µm, on a 15 µm thick quartz substrate. Once fabrication was completed, the individual filter chips were deiced and singulated. To provide a waveguide interface to test the filter circuits, metallic E-plane split blocks with the appropriate channels to mount the filter circuits were designed and machined using Computer Numerical Control (CNC) tools. To reduce the metallic loss, the aluminum block is plated with 0.5 mirons of gold . The filter circuits are carefully assembled into the metallic channels with the aid of alignment keys included in the filter design, and the circuit is secured using conductive silver epoxy, H20E from EPO-TEK.

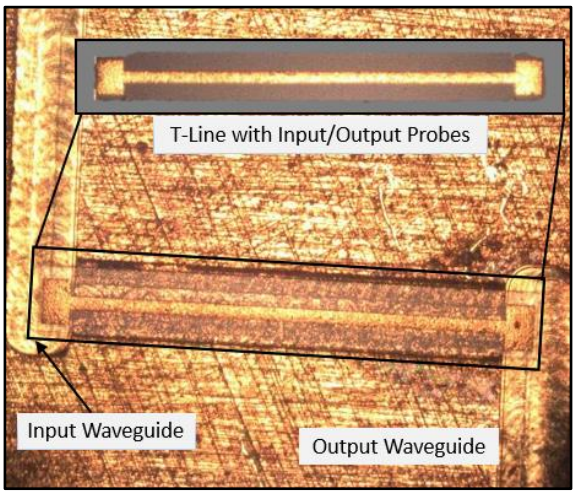

Figure 9: Fabricated and deiced throughline circuit with input and output probes integrated into waveguide channel.

Initially, a circuit with a Throughline similar to the filter structure is assembled into a metallic block with waveguide structures for performance comparison. Figure 9 illustrates a throughline design operating within the 500-750 GHz frequency range. The circuit is integrated into a channel of a waveguide block, with its mounting positioned on the bottom side of the block. Upon completion of the assembly, the upper section of the E-plane split block is used to enclose the structure securely.

Figure 10, a similar assembly process is implemented as the Throughline circuit to assemble the patch filter circuit. Figure 11 illustrates the assembled metallic housing of the filter, which has 20 × 20 × 7 mm dimensions. The structure incorporates a standard input/output waveguide and features waveguide interfaces that facilitate connections to extender modules for testing purposes.

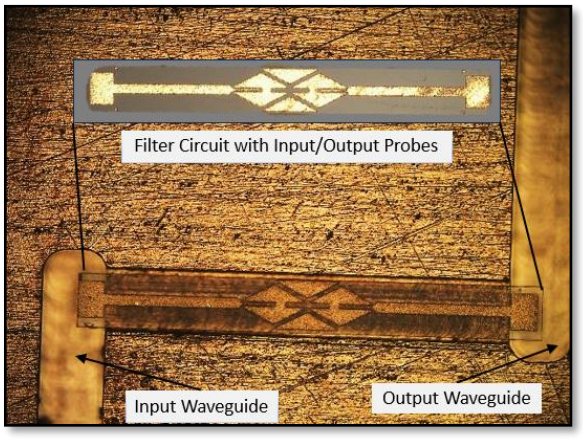

Figure 10: A fabricated and assembled high-order filter internal circuit with integrated waveguide probes.

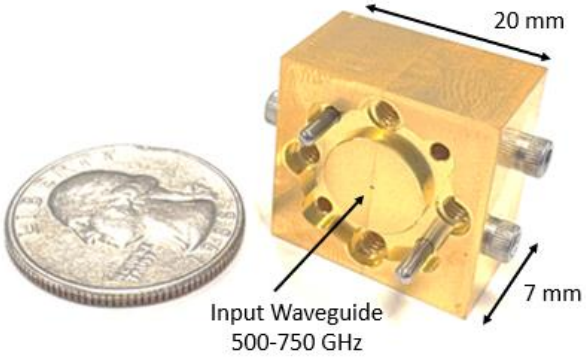

Figure 11: Assembled waveguide structures, including alignment pins, ready for RF testing.

IV. Filter Characterization and Results

The filter is characterized using Virginia Diode's (VDI) WR-1.5 (WM-380) frequency extender modules with Vector Network Analyzer (VNA). During the measurement, the filter is positioned between two extender modules connected to reference plane waveguide flanges (UG-387), as illustrated in Figure 12. The four alignment pins (two pins from each side) on the waveguide flanges facilitate precise alignment of the filter waveguide with the frequency-extender modules, ensuring optimal performance and accuracy. A Thru-Reflect-Line (TRL) standards are used to calibrate the VNA system at the frequency-extender module waveguide ports.

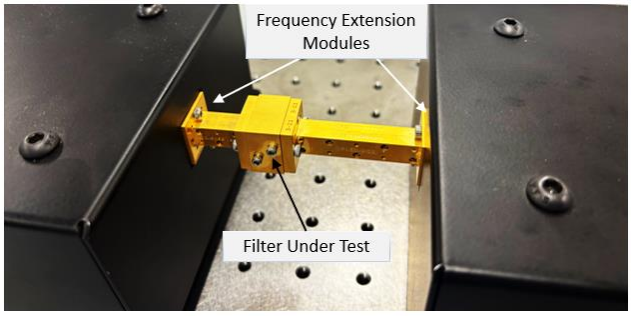

Figure 12: Filter test setup using frequency extension modules driven by VNA to characterize s-parameters.

In order to accurately assess the insertion loss of the filter structure in isolation, it is necessary to estimate the losses associated with the waveguide and probe structures. To facilitate this analysis, we measured the transmission response of a circuit incorporating a Throughline of comparable length and waveguide probes to those utilized in the filter. As illustrated in Figure 13, an Insertion Loss (S_{21}) of 2.9 dB and a Return Loss (S_{11}) of 15 dB were observed for the Throughline within the filter passband of 530-610 GHz. This loss is predominantly a result of conductive losses present in both the waveguide architecture and filter circuits with a finite gold conductivity of ~38×10^6 S/m.

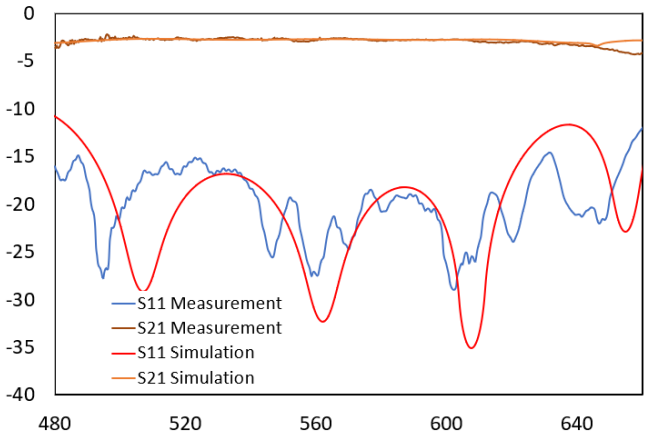

Figure 13: Measured and simulated S-parameters of the microwave through-line and waveguide probe structures.

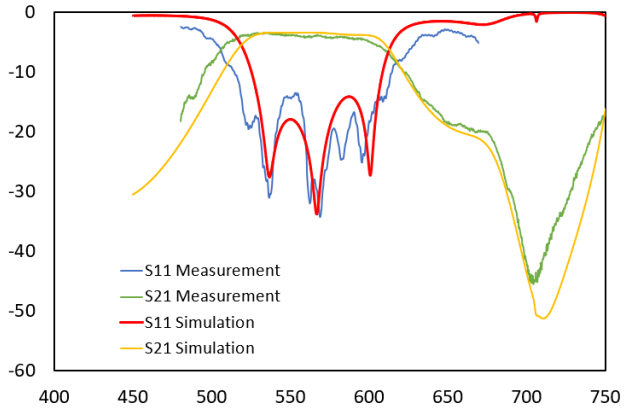

Figure 14. S-parameter measurement of the bandpass filter compared with a simulated performance.

Similarly, we characterized the S-parameter performance of the assembled filter. Figure 14 shows the fabricated filter's S_{11} and S_{21} performance, which demonstrates good agreement with the simulation. Further analysis of the measured responses revealed several factors that altered the performance from the optimized simulation shown in Figure 7. First, changes in the photomask compensation factor during the planar circuit fabrication for the gold metallization affected the results. Second, the waveguide structures exhibited CNC machining errors, contributing to the observed variations. Finally, the assembly process presented challenges in accurately positioning the filter input and output probes, primarily due to the reliance on freehand positioning methods, resulting in additional variations between the simulation and measured data. Thus, we adjusted our simulation to ensure accurate prediction of filter performance by incorporating the as build geometry in the model. The deviations in the fabricated circuits (± 0.5 µm), waveguide structure tolerance (± 5 µm), and 3-5 µm error due to the positions of the circuit relative to the waveguide were observed. With these updates, the filter response agreed well with the simulation. An additional slight difference at 556.936 GHz is due to the measurements' broad atmospheric water line. The filter response exhibited an S_{11} of -18dB, which meets our requirement of -15 dB. However, our initial investigation of the dimensional changes will leave us room for the next round of fabrications to improve filter performance closer to the optimized performance.

To isolate the loss attributed solely to the filter structure, we calculated the difference between the throughline insertion loss (2.9 dB) and the filter structure with probes (3.8 dB). This analysis reveals an estimated insertion loss of 0.9 dB due to the patch filter alone. In the context of our Single Sideband (SSB) receiver design, where the filter's primary function is to eliminate the image frequency band, this 0.9 dB loss represents significantly better performance compared to typical Double Sideband (DSB) receivers, which inherently suffer from a 3 dB noise increase. Furthermore, the filter design can be scaled for applications above 2 THz, where conventional approaches such as CNC or micromachined waveguides fail to provide viable solutions.

V. Conclusion

In this work, we have designed, fabricated, and characterized a novel compact bandpass filter employing patch resonators for operation in the 530-610 GHz frequency range. The filter demonstrates excellent performance with minimal insertion loss (<0.9 dB) and a return loss of better than 18 dB throughout the passband, combined with steep roll-off characteristics and wide rejection bands below 530 GHz and above 610 GHz. This compact structure is readily integrable with mixers and multiplier chips as part of a comprehensive circuit design strategy to suppress unwanted spurious signals effectively. The planar circuit approach presented here offers significant advantages, including cost-effectiveness, scalability to frequencies up to 2 THz, and straightforward tunability of the center frequency and bandwidth. These features make the filter particularly valuable for diverse applications spanning astronomy, defense systems, and high-frequency wireless communications. The demonstrated performance and design methodology represent a significant advancement in submillimeter-wave and THz filter technology, addressing critical needs in systems where conventional waveguide implementations face fundamental limitations.

VI. Acknowledgment

The work is funded by NASA Goddard Space Flight Center Internal Research and Development (IRAD) under projects “Silicon Micromachining for Millimeter and Submillimeter-Wave Application” and “Integrated Flexible Imaging CMOS Submillimeter-Wave Spectrometers for Solar System Exploration and Earth Science Atmospheric Studies.” The authors would like to thank Paul Racette (GSFC), Gordon Chain (GSFC), and Jeffrey Hasler (VDI) for their valuable discussions and insights.

VII. Reference

[1] P. M. Raphika, P. Abdulla, and P. M. Jasmine, "Compact lowpass filter with a sharp roll-off using patch resonators," Microw. Opt. Technol. Lett., vol. 56, no. 11, pp. 2534–2536, Nov. 2014, doi: 10.1002/mop.28644.

[2] M. Mirzaee and B. S. Virdee, "Realization of highly compact planar lowpass filter for UWB RFID applications," Electron. Lett., vol. 49, no. 22, pp. 1396–1398, Oct. 2013, doi: 10.1049/el.2013.2409.

[3] M. Mirzaee and B. S. Virdee, "Compact lowpass filter with high out-of-band rejection and super wide stopband performance," Microw. Opt. Technol. Lett., vol. 56, no. 4, pp. 947–950, Apr. 2014.

[4] J.-S. Hong and M. J. Lancaster, "Microstrip triangular patch resonator filters," in IEEE MTT-S Int. Microw. Symp. Dig., Boston, MA, USA, 2000, pp. 331–334, doi: 10.1109/MWSYM.2000.861002.

[5] R. B. Hammond, "HTS wireless filters: past present and future performance," Microw. J., vol. 41, no. 10, pp. 94–107, Oct. 1998.

[6] R. B. Hammond et al., "EETS wireless filters: past, present and future performance," Microw. J., vol. 41, no. 10, pp. 94–107, Oct. 1998.

[7] Z. Zhu, W. Hu, K. Xu, Y. Bai, and S. Li, "A W-band Chebyshev waveguide bandpass filter with wide stopband performance," Electronics, vol. 13, no. 9, p. 1793, Apr. 2024, doi: 10.3390/electronics13091793.

[8] K. M. K. H. Leong et al., "WR1.5 silicon micromachined waveguide components and active circuit integration methodology," IEEE Trans. Microw. Theory Techn., vol. 60, no. 4, pp. 998–1005, Apr. 2012, doi: 10.1109/TMTT.2012.2184296.

[9] D. Wang, M. J. Lancaster, Y. Wang, K. M. Shum, and Q. Zhang, "WR-1.5 (500–750 GHz) waveguide bandpass filter fabricated using high precision computer numerically controlled machining," Microw. Opt. Technol. Lett., vol. 62, no. 1, pp. 1–5, Jan. 2020.

[10] X. Shang, Y. Tian, M. J. Lancaster, and J. Zhou, "A SU8 micromachined WR-1.5 band waveguide filter," IEEE Microw. Wireless Compon. Lett., vol. 23, no. 6, pp. 300–302, Jun. 2013.

[11] J. Hu, S. Liu, and Y. Zhang, "Micromachined terahertz rectangular waveguide bandpass filter on silicon-substrate," IEEE Microw. Wireless Compon. Lett., vol. 22, no. 12, pp. 636–638, Dec. 2012.

[12] D. W. Porterfield, "WM380 (675–700 GHz) bandpass filters in milled, split-block construction," in IEEE MTT-S Int. Microw. Symp. Dig., Honolulu, HI, USA, 2007, pp. 1191–1194.

[13] Z. Zheng, J. Hu, S. Liu, and Y. Fan, "Micromachined terahertz waveguide band-pass filters," in IEEE Int. Conf. Commun. Problem-Solving (ICCP), Taipei, Taiwan, 2016, pp. 1–3.

[14] H. Li, Y. Fan, J. Hu, and S. Liu, "Copper micromachined WR-2.2 band waveguide and bandpass filter," Microw. Opt. Technol. Lett., vol. 64, no. 4, pp. 1022–1026, Apr. 2022.

[15] Y. Wu, Z. Hao, R. Lu, and W. Hong, "A high-selectivity D-band mixed-mode filter based on the coupled overmode cavities," IEEE Trans. Microw. Theory Techn., vol. 68, no. 6, pp. 2196–2208, Jun. 2020.

[16] M. M. Gohari, O. Glubokov, and J. Oberhammer, "Ultra-narrowband silicon-micromachined sub-THz filter with wide spurious-free rejection band employing high-Q TM330 resonators," IEEE Trans. Microw. Theory Techn., vol. 71, no. 3, pp. 1211–1221, Mar. 2023.

[17] O. Glubokov, X. Zhao, J. Campion, U. Shah, and J. Oberhammer, "Micromachined filters at 450 GHz with 1% fractional bandwidth and unloaded Q beyond 700," IEEE Trans. THz Sci. Technol., vol. 9, no. 1, pp. 106–108, Jan. 2019.

[18] Lamb, James W. "SSB vs. DSB for Submillimeter Receivers." ALMA Memo 301, National Radio Astronomy Observatory, (2000): 1-6.

[19] Goldsmith, P. F. "Quasi-Optical Systems: Gaussian Beam Quasi-Optical Propagation and Applications (Piscataway, NJ: IEEE)." (1998).

[20] S. A. Maas, *Microwave Mixers*, 2nd ed. Norwood, MA, USA: Artech House, 1993.